Damping Characteristic Analysis of Wind-thermal-bundled Systems

Shiying Ma, *Member*, *IEEE* and Liwen Zheng

***Abstract*—Wind-thermal-bundled system has emerged as the predominant type of power system, incorporating a significant proportion of renewable energy. The dynamic interaction mechanism of the system is complex, and the issue of oscillation stability is significant. In this paper, the damping characteristics of the direct current (DC) capacitance oscillation mode are analyzed using the path analysis method (PAM). This method combines the transfer-function block diagram with the damping torque analysis (DTA). Firstly, the linear models of the permanent magnet synchronous generator (PMSG), the synchronous generator (SG), and the alternating current (AC) grid are established based on the transfer functions. The closed-loop transfer-function block diagram of the wind-thermal-bundled systems is derived. Secondly, the block diagram reveals the damping path and the dynamic interaction mechanism of the system. According to the superposition principle, the transfer-function block diagram is reconstructed to achieve the damping separation. The damping coefficient of the DTA is used to quantify the effect of the interaction between the subsystems on the damping characteristics of the oscillation mode. Then, the eigenvalue analysis is used to analyze the system stability. Finally, the damping characteristic analysis is validated by time-domain simulations.**

***Index Terms*—Wind-thermal-bundled system, path analysis method (PAM), transfer-function block diagram, damping.**

NOMENCLATURE

A. Variables

ω_g	Grid frequency
ω_0	Rated frequency
δ, ω	Power angle and frequency of synchronous generator (SG)
$\Delta\theta_{PLL}$	Phase locked loop (PLL) output angle
$\Delta\boldsymbol{X}$	State variable matrix
$\Delta\boldsymbol{u}$	Input variable matrix
$\boldsymbol{A}$	Coefficient matrix
$\boldsymbol{B}$	Input matrix
C_1	Line capacitance
C_{dc}	Direct current (DC) capacitance between machine-side converter (MSC) and grid-side converter (GSC)
E_{fd}	Forced no-load electromotive force of SG
E'_q	q-aixs transient electromotive force of SG
F_{HP}	Power proportional coefficient of high-pressure cylinder
$H_{PLL}(s)$	Transfer function from Δu_{gq} to $\Delta\theta_{pll}$
K_δ	Reciprocal of unequal rate
K_p	Proportional coefficient of proportional-integral-derivative (PID) link in governor system
K_{pdc}, K_{idc}	Proportional and integral coefficients of constant DC voltage control
k_{pPLL}, k_{iPLL}	Proportional coefficient and integral coefficient of PLL
M, D	Inertia and damping coefficients of SG
P_e	Input power of GSC
P_{in}	Output active power of MSC
P_m, P_t	Mechanical power and electromagnetic power of SG
R_1, L_1, i_1	Grid-side resistance, inductance, and current of permanent magnet synchronous generator (PMSG)
R_2, L_2	Equivalent resistance and inductance of alternating current (AC) grid
R_g, L_g	Filter resistance and inductance of PMSG
R_o, L_o	Resistance and inductance of grid-connected line
R, X'_q	Resistance and q-axis transient reactance of SG
T_1	Time constant of hydraulic motor
T_{CH}	Time constant of steam chest
T'_{d0}	d-axis transient time constant of SG
U_{dc}	Voltage of DC capacitance
U_{dcref}	Voltage reference value of DC capacitance
u_2, i_2	Voltage and current of AC grid
u_g	Voltage of line capacitance
u_s, i_s	Stator voltage and current of wind turbine (WT)

Manuscript received: September 5, 2023; revised: January 8, 2024; accepted: April 16, 2024. Date of CrossCheck: April 16, 2024. Date of online publication: May 10, 2024.

This work was supported in part by National Key R&D Program of China (No. 2022YFB2403100).

S. Ma and L. Zheng (corresponding author) are with the Power System Department, China Electric Power Research Institute, Beijing 100192, China (e-mail: msy_1969@163.com; 18713591731@163.com).

DOI: 10.35833/MPCE.2023.000639

u_t, i_g	Output voltage and current of GSC
u_r	Voltage at point of common coupling (PCC)
u_o, i_o	Output voltage and current of SG
X_d, X'_d	d-axis reactance and d-axis transient reactance of SG

B. Subscripts

d, q	d-axis and q-axis components of rotating reference frame signal
d_2, q_2	d_2-axis and q_2-axis components of rotating reference frame signal
ref, 0	Reference and steady-state values of variable
x, y	x-axis and y-axis components of rotating reference frame signal

I. Introduction

In China, wind farms are mainly concentrated in the western, northern, and eastern coastal areas. The wind power and thermal power are transmitted to central load centers through high-capacity, long-distance transmission systems [1]. In addition, the permanent magnet synchronous generator (PMSG) has gradually become the dominant model for wind farms due to its high efficiency and low failure rate [2]. Thus, the wind-thermal-bundled system is gradually emerging as one of the primary methods for wind energy supply, offering the advantages of low cost and high efficiency [3]. However, the grid-connected PMSG system consists of multiple power electronic devices and controllers, which can lead to oscillation problems [4]-[6]. It is of great scientific and engineering importance to investigate the damping characteristics of wind-thermal-bundled systems.

Currently, several methods are available to study system oscillations, including the eigenvalue method, impedance model analysis (IMA) method, open-loop mode resonance method, damping torque analysis (DTA) method, and time-domain simulation method [7]-[9].

1) The eigenvalue method based on the small-signal model is used to analyze the variables and subsystems related to the oscillation modes. Using the eigenvalue method, it has been found that PMSGs connected to the power system could reduce the system stability under small disturbances [10]. In [11], based on the participation factor (PF), it is found that PMSG does not contribute to the low-frequency oscillation (LFO) of the system, which contradicts the conclusion of [10].

2) The IMA method is a frequency domain method that explains the interaction mechanism between subsystems based on their external impedance characteristics. The effect of the PMSGs on the sub-synchronous torsional interactions (SSTI) of thermal power units is investigated by IMA, taking into account the field winding and damper winding of synchronous machines. It is shown that PMSGs can lead to insufficient damping of SSTI [12].

3) The open-loop-mode resonance analysis method has investigated the mechanism of strong interaction by studying the open-loop-mode coupling. It is found that the simultaneous involvement of the PMSG and synchronous generator (SG) in oscillation modes is due to the proximity of the converter oscillation mode (COM) and the electromechanical oscillation mode (EOM) [13]. In [14], [15], modal resonance occurs when the open-loop mode of the phase-locked loop (PLL) and the open-loop mode of the power system approach on the complex plane, which degrades the damping of the oscillation modes.

4) In the DTA method, the studied system is equated to be second-order due to the similarity between the system and the rotor motion equation of the SG. The damping torque coefficient is used to study the vibration characteristics of the system. In [16], based on the rotor motion equation, the voltage source converter (VSC) model is presented to describe its internal voltage dynamics in the time scale of the direct current (DC)-link voltage control.

However, the eigenvalue analysis and open-loop mode resonance analysis methods suffer from the "dimensional disaster" problem and are unable to analyze the transmission path of frequency disturbances. IMA can explain the vibration mechanism at the physical level and can be used to model the "black (gray) box" system. However, it is difficult to uncover the dynamic interactions within the system from the external impedance characteristics of the device alone. The DTA method can only study the damping characteristics of the system itself and cannot separate the dynamics of the interactions between the various links in the system. The differential algebraic equation (DAE) is used to describe the system dynamics in time-domain simulation methods, but it cannot reveal the oscillation coupling mechanism. Time-domain simulation method can be used to verify the validity of the theoretical analysis. Given the limitations of the above methods, it is crucial to explore the dynamic interaction mechanism from a new perspective.

The DTA [17]-[19], IMA [20], and open-loop-mode resonance [21], [22] methods have been used for the analysis of the DC capacitance-dominated oscillation modes in power systems. In [17]-[19], the dynamic DC capacitance is expressed as a second-order differential equation, and the DTA method is used to analyze the stability of the DC capacitance. The definitions of equivalent inertia, synchronization power, and damping power are also discussed. It is found that the insufficient positive synchronization and damping power can lead to the instability. In [23]-[25], small-signal models of the PMSG and the doubly-fed induction generator (DFIG) are established to study the stability of the DC-link voltage. However, the dynamic interaction mechanism between the subsystems has not been revealed, and the effect of various interactions on the damping of oscillation modes cannot be quantified. To address this issue, the stability of the DC capacitance oscillation mode and the PLL oscillation mode have been investigated using the transfer-function block diagram and the damping separation method [26]-[30]. It has been found that the DC capacitance-dominated sub-synchronous oscillation (SSO) is more prone to instability when the PMSG is connected to a weak alternating current (AC) grid or a line-commutated converter-based high-voltage direct current (LCC-HVDC) system [26]-[28]. However, the external AC grid is equivalent to a voltage source, and

the dynamics of the SG are not involved [26]-[30]. It is essential to develop the SG model to analyze the damping characteristics of wind-thermal-bundled systems.

In this paper, the path analysis method (PAM) is used to analyze the stability of the DC capacitance oscillation mode by combining the transfer-function block diagram and DTA. Compared with other methods, PAM can elucidate the path of disturbance transmission and the coupling relationships between the subsystems. The effect of the interaction between the subsystems on the damping of the oscillation modes is quantified by the damping reconstruction. The contributions of this paper include the following aspects.

1) The linear models (LMs) of the PMSG, SG, and AC grid are established using the transfer function equations, and the closed-loop transfer-function block diagram of the wind-thermal-bundled system is derived.

2) The closed-loop transfer-function block diagram shows the damping path and the dynamic interaction process of the subsystem. The block diagram is reconstructed to achieve damping separation based on the superposition principle. The DTA method is used to quantify the effect of dynamic interaction between subsystems on the DC capacitance oscillation mode.

3) The effect of system parameters on the damping of the DC capacitance oscillation mode is analyzed using the damping separation method and the eigenvalue method, and verified by time-domain simulation.

The remainder of this paper is organized as follows. In Section II, the LM for the wind-thermal-bundled system is established, and the transfer-function block diagram is obtained. Sections III and IV conduct damping characteristic analyses based on PAM and eigenvalue analysis method, respectively. Section III shows the coupling relationships between the subsystems based on the block diagram, which is constructed to achieve damping separation. In Section IV, the state-space model of the wind-thermal-bundled system is established, and the oscillation mode of the system is analyzed with varying parameters. In Section V, the effect of the system parameters on the damping of the DC capacitance oscillation mode is confirmed by simulation results. Conclusions are given in Section VI.

II. LM for Wind-Thermal-Bundled System

In this section, the transfer function equations are used to establish the LMs of the PMSG, SG, and AC grid. Then, the transfer-function block diagram of the wind-thermal-bundled system is derived, and its validity is verified by the step response characteristics of the electromagnetic transient model (ETM). The diagram of the wind-thermal-bundled system is shown in Fig. 1.

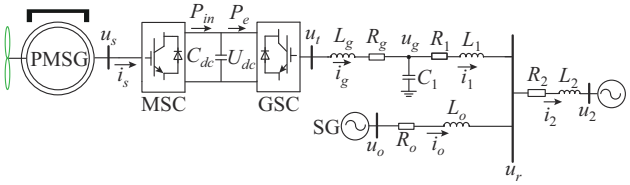

Fig. 1. Diagram of wind-thermal-bundled system.

In the following, the voltage $\boldsymbol{u}_r$ is used as an example, and $\boldsymbol{u}_r=\left[u_{rx};u_{ry}\right]$, $\boldsymbol{u}_{rdq}=\left[u_{rd};u_{rq}\right]$, $\boldsymbol{u}_{rd2q2}=\left[u_{rd2};u_{rq2}\right]$.

A. LM of PMSG

The PMSG subsystem consists of the DC capacitance, the GSC, the PLL, the filter inductance, and the grid-connected transmission lines. The control diagram of the GSC is shown in Fig. 2.

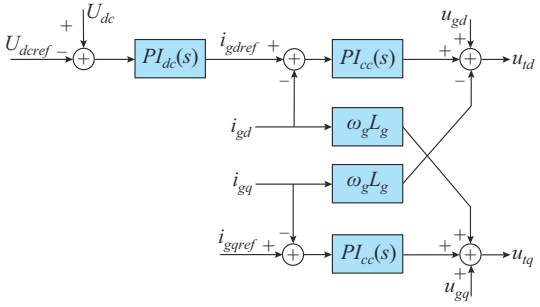

Fig. 2. Control diagram of GSC.

In Fig. 2, $PI_{dc}(s)$ and $PI_{cc}(s)$ are the DC voltage outer loop control and the current inner loop control, respectively.

The dynamics of the constant DC voltage outer loop control for the GSC are given as:

$$\begin{cases}\Delta i_{gdref}=PI_{dc}(s)\,\Delta U_{dc}\\ \Delta i_{gqref}=0\end{cases} \tag{1}$$

where $PI_{dc}(s)=K_{pdc}+K_{idc}/s$.

The bandwidth of the DC voltage outer loop is designed to be one-tenth of the bandwidth of the current inner loop. Therefore, the grid-side current can follow its reference value based on the current inner loop. It can be expressed as $\Delta i_{gd}=\Delta i_{gdref}$ and $\Delta i_{gq}=\Delta i_{gqref}$. As the power factor of the GSC is 1, Δi_{gqref} is set to be 0. Then, both Δi_{gq} and i_{gq} are equal to 0. So, the output active power of the GSC is:

$$\Delta P_e=1.5\left(u_{td0}\Delta i_{gd}+i_{gd0}\Delta u_{td}\right)=\boldsymbol{G}_1\begin{bmatrix}\Delta i_{gd}\\ \Delta u_{td}\end{bmatrix} \tag{2}$$

where $\boldsymbol{G}_1$ is the transfer function matrix from Δi_{gd} and Δu_{td} to ΔP_e. The expression for $\boldsymbol{G}_1$ is given in (A1) in Appendix A.

The dynamic equation for the DC capacitance is:

$$\begin{cases}\Delta U_{dc}=G_{dc}(s)\left(\Delta P_{in}-\Delta P_e\right)\\ G_{dc}(s)=\dfrac{1}{sC_{dc}U_{dc0}}\end{cases} \tag{3}$$

The dynamic equation for the PLL is:

$$\Delta\theta_{PLL}=\frac{k_{iPLL}+sk_{pPLL}}{s^2}\Delta u_{gq}=H_{PLL}(s)\,\Delta u_{gq} \tag{4}$$

The filter line dynamics are:

$$\begin{bmatrix}\Delta u_{td}\\ \Delta u_{tq}\end{bmatrix}=\begin{bmatrix}\Delta u_{gd}\\ \Delta u_{gq}\end{bmatrix}+\begin{bmatrix}R_g+sL_g & -\omega_g L_g\\ \omega_g L_g & R_g+sL_g\end{bmatrix}\begin{bmatrix}\Delta i_{gd}\\ \Delta i_{gq}\end{bmatrix} \tag{5}$$

In (5), Δu_{td} can be written as:

$$\Delta u_{td}=\boldsymbol{G}_2(s)\begin{bmatrix}\Delta i_{gd}\\ \Delta u_{gd}\end{bmatrix} \tag{6}$$

where $\boldsymbol{G}_2(s)$ is the transfer function matrix from Δi_{gd} and

Δu_{gd} to Δu_{td}. The expression for $\boldsymbol{G}_2(s)$ is given in (A2) in Appendix A.

The dynamic equations for the capacitance and impedance of the lines connected with the network are given as:

$$\begin{bmatrix}\Delta u_{gx}\\ \Delta u_{gy}\end{bmatrix}=\boldsymbol{G}_3(s)\begin{bmatrix}\Delta i_{gx}\\ \Delta i_{gy}\end{bmatrix}+\boldsymbol{G}_4(s)\begin{bmatrix}\Delta i_{1x}\\ \Delta i_{1y}\end{bmatrix} \tag{7}$$

$$\begin{bmatrix}\Delta i_{1x}\\ \Delta i_{1y}\end{bmatrix}=\boldsymbol{G}_5(s)\begin{bmatrix}\Delta u_{gx}\\ \Delta u_{gy}\end{bmatrix}+\boldsymbol{G}_6(s)\begin{bmatrix}\Delta u_{rx}\\ \Delta u_{ry}\end{bmatrix} \tag{8}$$

where $\boldsymbol{G}_3(s)$ and $\boldsymbol{G}_4(s)$ are the transfer function matrices from $\Delta \boldsymbol{i}_g$ and $\Delta \boldsymbol{i}_1$ to $\Delta \boldsymbol{u}_g$, respectively; $\boldsymbol{G}_5(s)$ and $\boldsymbol{G}_6(s)$ are the transfer function matrices from $\Delta \boldsymbol{u}_g$ and $\Delta \boldsymbol{u}_r$ to $\Delta \boldsymbol{i}_1$, respectively; and the expressions for $\boldsymbol{G}_3(s)$-$\boldsymbol{G}_6(s)$ are given in (A3) and (A4) in Appendix A.

For $\boldsymbol{u}_g$ and $\boldsymbol{i}_g$, the transformation equations between the x-y frame and the d-q frame are:

$$\begin{bmatrix}\Delta u_{gd}\\ \Delta u_{gq}\end{bmatrix}=\boldsymbol{T}_{ug}\begin{bmatrix}\Delta u_{gx}\\ \Delta u_{gy}\\ \Delta\theta_{PLL}\end{bmatrix} \tag{9}$$

$$\begin{bmatrix}\Delta i_{gx}\\ \Delta i_{gy}\end{bmatrix}=\boldsymbol{T}_{ig}\begin{bmatrix}\Delta i_{gd}\\ \Delta i_{gq}\\ \Delta\theta_{PLL}\end{bmatrix} \tag{10}$$

where $\boldsymbol{T}_{ug}$ is the transfer function matrix from $\Delta \boldsymbol{u}_g$ and $\Delta\theta_{PLL}$ to $\Delta \boldsymbol{u}_{gdq}$; and $\boldsymbol{T}_{ig}$ is the transfer function matrix from $\Delta \boldsymbol{i}_{gdq}$ and $\Delta\theta_{PLL}$ to $\Delta \boldsymbol{i}_g$. The detailed expressions of $\boldsymbol{T}_{ug}$ and $\boldsymbol{T}_{ig}$ are given in (A5) and (A6) in Appendix A.

Combining (7), (8), and (10) yields $\Delta \boldsymbol{i}_1$:

$$\begin{bmatrix}\Delta i_{1x}\\ \Delta i_{1y}\end{bmatrix}=\boldsymbol{G}_7(s)\begin{bmatrix}\Delta i_{gd}\\ \Delta\theta_{PLL}\\ \Delta u_{rx}\\ \Delta u_{ry}\end{bmatrix} \tag{11}$$

where $\boldsymbol{G}_7(s)$ is the transfer function matrix from Δi_{gd}, $\Delta\theta_{PLL}$, $\Delta \boldsymbol{u}_r$ to $\Delta \boldsymbol{i}_1$. As $\boldsymbol{G}_7(s)$ is complicated, it will not be listed in this paper.

Combining (7), (9), and (10), we can obtain $\Delta \boldsymbol{u}_{gdq}$ as:

$$\begin{bmatrix}\Delta u_{gd}\\ \Delta u_{gq}\end{bmatrix}=\boldsymbol{G}_8(s)\begin{bmatrix}\Delta i_{gd}\\ \Delta\theta_{PLL}\\ \Delta i_{1x}\\ \Delta i_{1y}\end{bmatrix} \tag{12}$$

where $\boldsymbol{G}_8(s)$ is the transfer function matrix from Δi_{gd}, $\Delta\theta_{PLL}$, $\Delta \boldsymbol{i}_1$ to $\Delta \boldsymbol{u}_{gdq}$.

Based on (1) - (4), (6), (11), and (12), the LM of the PMSG is shown in Fig. 3. The input variables are Δu_{rx}, Δu_{ry}, and ΔP_{in}, while the output variables are Δi_{1x} and Δi_{1y}.

B. LM of SG

The voltage equation for SG is given as:

$$\begin{cases}\Delta u_{od_2}=-R\Delta i_{od_2}-X_q'\Delta i_{oq_2}\\ \Delta u_{oq_2}=\Delta E_q'-R\Delta i_{oq_2}+X_d'\Delta i_{od_2}\end{cases} \tag{13}$$

The third-order dynamic model of SG is given as:

$$\begin{cases}s\Delta\delta=\omega_0\Delta\omega\\ Ms\Delta\omega=\Delta P_m-\Delta P_t-D\Delta\omega\\ T_{d0}'s\Delta E_q'=\Delta E_{fd}-\Delta E_q'+\left(X_d-X_d'\right)\Delta i_{od_2}\end{cases} \tag{14}$$

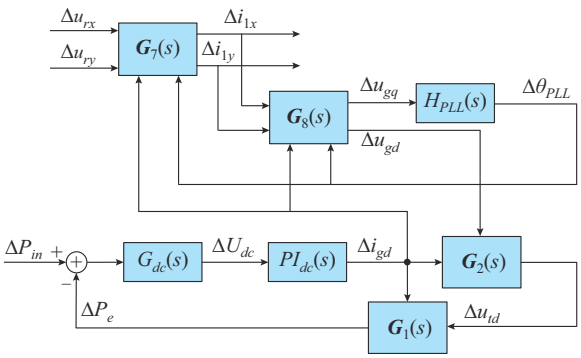

Fig. 3. LM of PMSG.

Considering the governor and turbine of SG, the relationship between the $\Delta\omega$ and ΔP_m is:

$$\Delta P_m=-\frac{F_{HP}K_pK_\delta}{\left(1+T_1s\right)\left(1+T_{CH}s\right)}\Delta\omega=-G_{\omega\text{-}P_m}(s)\Delta\omega \tag{15}$$

In the d_2-q_2 frame, the dynamic equation of the SG grid-connected transmission line is:

$$\begin{bmatrix}\Delta u_{od_2}\\ \Delta u_{oq_2}\end{bmatrix}=\begin{bmatrix}\Delta u_{rd_2}\\ \Delta u_{rq_2}\end{bmatrix}+\begin{bmatrix}R_o+sL_o & -\omega_gL_o\\ \omega_gL_o & R_o+sL_o\end{bmatrix}\begin{bmatrix}\Delta i_{od_2}\\ \Delta i_{oq_2}\end{bmatrix} \tag{16}$$

Combining (13) and (16), we can obtain:

$$\begin{bmatrix}\Delta i_{od_2}\\ \Delta i_{oq_2}\end{bmatrix}=\begin{bmatrix}-R-R_o-sL_o & -X_q'+\omega_gL_o\\ X_d'-\omega_gL_o & -R-R_o-sL_o\end{bmatrix}^{-1}\begin{bmatrix}\Delta u_{rd_2}\\ \Delta u_{rq_2}-\Delta E_q'\end{bmatrix} \tag{17}$$

Substituting (13) and (17) into the third formula of (14), we can obtain:

$$\Delta E_q'=\boldsymbol{G}_9(s)\begin{bmatrix}\Delta u_{rd_2}\\ \Delta u_{rq_2}\end{bmatrix} \tag{18}$$

where $\boldsymbol{G}_9(s)$ is the transfer function matrix from $\Delta \boldsymbol{u}_{rd_2q_2}$ to $\Delta E_q'$, and the detailed expression of $\boldsymbol{G}_9(s)$ is given in (A7) in Appendix A.

By substituting (18) into (16), $\Delta \boldsymbol{i}_{od_2q_2}$ can be written as:

$$\begin{bmatrix}\Delta i_{od_2}\\ \Delta i_{oq_2}\end{bmatrix}=\boldsymbol{G}_{10}(s)\begin{bmatrix}\Delta u_{rd_2}\\ \Delta u_{rq_2}\end{bmatrix} \tag{19}$$

where $\boldsymbol{G}_{10}(s)$ is the transfer function from $\Delta \boldsymbol{u}_{rd_2q_2}$ to $\Delta \boldsymbol{i}_{od_2q_2}$, and the detailed expression of $\boldsymbol{G}_{10}(s)$ is given in (A8) in Appendix A.

The active power of SG is:

$$\Delta P_t=u_{od_20}\Delta i_{od_2}+i_{od_20}\Delta u_{od_2}+u_{oq_20}\Delta i_{oq_2}+i_{oq_20}\Delta u_{oq_2} \tag{20}$$

By substituting (16) and (19) into (20), ΔP_t is obtained as:

$$\Delta P_t=\boldsymbol{G}_{11}(s)\begin{bmatrix}\Delta u_{rd_2}\\ \Delta u_{rq_2}\end{bmatrix} \tag{21}$$

where $\boldsymbol{G}_{11}(s)$ is the transfer function matrix from $\Delta \boldsymbol{u}_{rd_2q_2}$ to ΔP_t.

For Δu_r and Δi_o, the conversion relation between the d_2-q_2 frame and the x-y frame is given as:

$$\begin{bmatrix}\Delta u_{rd_2}\\ \Delta u_{rq_2}\end{bmatrix}=\boldsymbol{G}_{12}\begin{bmatrix}\Delta u_{rx}\\ \Delta u_{ry}\\ \Delta\delta\end{bmatrix} \tag{22}$$

$$\begin{bmatrix}\Delta i_{ox}\\ \Delta i_{oy}\end{bmatrix}=\boldsymbol{G}_{13}\begin{bmatrix}\Delta i_{od_2}\\ \Delta i_{oq_2}\\ \Delta\delta\end{bmatrix} \tag{23}$$

where $\boldsymbol{G}_{12}$ is the transfer function matrices from $\Delta\boldsymbol{u}_r$ and $\Delta\delta$ to $\Delta\boldsymbol{u}_{rd_2q_2}$; and $\boldsymbol{G}_{13}$ is the transfer function matrices from $\Delta\boldsymbol{i}_{od_2q_2}$ and $\Delta\delta$ to $\Delta\boldsymbol{i}_o$. The detailed expressions of $\boldsymbol{G}_{12}$ and $\boldsymbol{G}_{13}$ are given in (A9) and (A10) in Appendix A, respectively.

Based on (14), (19), (21)-(23), the LM of SG is shown in Fig. 4. The input variables are Δu_{rx} and Δu_{ry}, while the output variables are Δi_{ox} and Δi_{oy}.

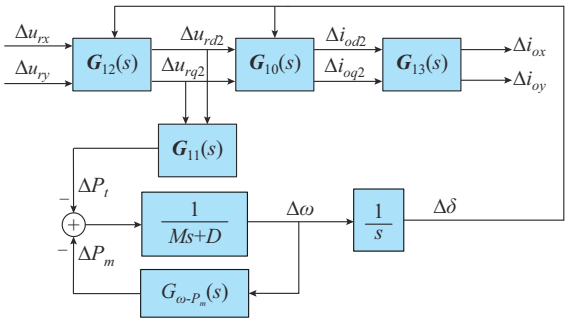

Fig. 4. LM of SG.

C. LM of AC Grid

The dynamics of the AC grid are given as:

$$\begin{bmatrix}\Delta i_{2x}\\ \Delta i_{2y}\end{bmatrix}=\boldsymbol{G}_{14}(s)\begin{bmatrix}\Delta u_{rx}\\ \Delta u_{ry}\end{bmatrix}+\boldsymbol{G}_{15}(s)\begin{bmatrix}\Delta u_{2x}\\ \Delta u_{2y}\end{bmatrix} \tag{24}$$

where $\boldsymbol{G}_{14}(s)$ and $\boldsymbol{G}_{15}(s)$ are the transfer function matrices from $\Delta\boldsymbol{u}_r$ and $\Delta\boldsymbol{u}_2$ to $\Delta\boldsymbol{i}_2$, respectively. The expressions of $\boldsymbol{G}_{14}(s)$ and $\boldsymbol{G}_{15}(s)$ are given in (A11) in Appendix A.

Omitting the change of $\Delta\boldsymbol{u}_2$, (24) can be rewritten as:

$$\begin{bmatrix}\Delta i_{2x}\\ \Delta i_{2y}\end{bmatrix}=\boldsymbol{G}_{14}(s)\begin{bmatrix}\Delta u_{rx}\\ \Delta u_{ry}\end{bmatrix} \tag{25}$$

According to Fig. 1, (26) is obtained as:

$$\begin{bmatrix}\Delta i_{2x}\\ \Delta i_{2y}\end{bmatrix}=\begin{bmatrix}\Delta i_{1x}\\ \Delta i_{1y}\end{bmatrix}+\begin{bmatrix}\Delta i_{ox}\\ \Delta i_{oy}\end{bmatrix} \tag{26}$$

The combination of (25) and (26) gives:

$$\begin{bmatrix}\Delta u_{rx}\\ \Delta u_{ry}\end{bmatrix}=\boldsymbol{G}_{16}(s)\left(\begin{bmatrix}\Delta i_{1x}\\ \Delta i_{1y}\end{bmatrix}+\begin{bmatrix}\Delta i_{ox}\\ \Delta i_{oy}\end{bmatrix}\right) \tag{27}$$

where $\boldsymbol{G}_{16}(s)$ is the transfer function matrix from $\Delta\boldsymbol{i}_1$ and $\Delta\boldsymbol{i}_o$ to $\Delta\boldsymbol{u}_r$. The detailed expression of $\boldsymbol{G}_{16}(s)$ is given in (A12) in Appendix A.

Based on (27), the aggregated LM of the AC grid is shown in Fig. 5. The input variables are $\Delta\boldsymbol{i}_o$ and $\Delta\boldsymbol{i}_1$, while the output variables are $\Delta\boldsymbol{u}_r$.

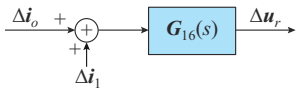

Fig. 5. Aggregated LM of AC grid.

D. Closed-loop Transfer Function Model

By combining (2), (3), (5), (11), and (12) to eliminate the intermediate variables Δi_1, $\Delta\theta_{PLL}$, Δi_g, and Δu_t, the output power of the PMSG is calculated as:

$$\Delta P_e=G_{p1}(s)\Delta U_{dc}+\boldsymbol{G}_{p2}(s)\begin{bmatrix}\Delta u_{rx}\\ \Delta u_{ry}\end{bmatrix} \tag{28}$$

where $G_{p1}(s)$ is the transfer function from ΔU_{dc} to ΔP_e; and $\boldsymbol{G}_{p2}(s)$ is the transfer function matrix from $\Delta\boldsymbol{u}_r$ to ΔP_e.

By combining (1), (4), (11), and (12) to eliminate the intermediate variables $\Delta\theta_{PLL}$ and Δi_g, $\Delta\boldsymbol{i}_1$ can be rewritten as:

$$\begin{bmatrix}\Delta i_{1x}\\ \Delta i_{1y}\end{bmatrix}=\boldsymbol{G}_{i1}(s)\Delta U_{dc}+\boldsymbol{G}_{i2}(s)\begin{bmatrix}\Delta u_{rx}\\ \Delta u_{ry}\end{bmatrix} \tag{29}$$

where $\boldsymbol{G}_{i1}(s)$ and $\boldsymbol{G}_{i2}(s)$ are the transfer function matrices from ΔU_{dc} and $\Delta\boldsymbol{u}_r$ to $\Delta\boldsymbol{i}_1$, respectively.

Based on (3), (28), and (29), the aggregated LM of the PMSG is shown in Fig. 6. The input variables are $\Delta\boldsymbol{u}_r$ and ΔP_{in}, while the output variables are $\Delta\boldsymbol{i}_1$.

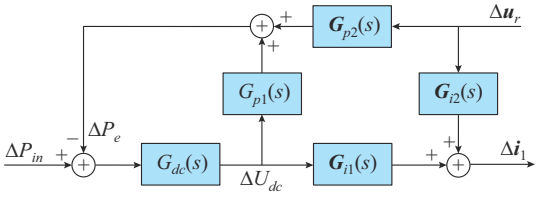

Fig. 6. Aggregated LM of PMSG.

By substituting (22) into (21), the active power of SG is obtained as:

$$\Delta P_t=G_{p3}(s)\Delta\delta+\boldsymbol{G}_{p4}(s)\begin{bmatrix}\Delta u_{rx}\\ \Delta u_{ry}\end{bmatrix} \tag{30}$$

where $G_{p3}(s)$ is the transfer function from $\Delta\delta$ to ΔP_t; and $\boldsymbol{G}_{p4}(s)$ is the transfer function matrix from $\Delta\boldsymbol{u}_r$ to ΔP_t. The detailed expressions of $G_{p3}(s)$ and $\boldsymbol{G}_{p4}(s)$ are given in (A13) in Appendix A.

Combining (19), (22), and (23), we can obtain:

$$\begin{bmatrix}\Delta i_{ox}\\ \Delta i_{oy}\end{bmatrix}=\boldsymbol{G}_{i3}(s)\Delta\delta+\boldsymbol{G}_{i4}(s)\begin{bmatrix}\Delta u_{rx}\\ \Delta u_{ry}\end{bmatrix} \tag{31}$$

where $\boldsymbol{G}_{i3}(s)$ and $\boldsymbol{G}_{i4}(s)$ are the transfer function matrices from $\Delta\delta$ and $\Delta\boldsymbol{u}_r$ to $\Delta\boldsymbol{i}_o$, respectively. The expressions of $\boldsymbol{G}_{i3}(s)$ and $\boldsymbol{G}_{i4}(s)$ are given in (A14) and (A15) in Appendix A, respectively.

Substituting (15) into (14), we obtain the transfer function from ΔP_t to $\Delta\delta$:

$$G_{P\text{-}\delta}(s)=\frac{1}{Ms^2+Ds+sG_{\omega\text{-}P_m}(s)} \tag{32}$$

Based on (14) and (30)-(32), the aggregated LM of SG is shown in Fig. 7. The input variables are $\Delta\boldsymbol{u}_r$, while the output variables are $\Delta\boldsymbol{i}_o$.

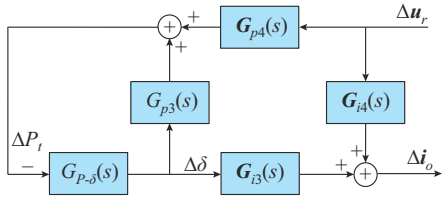

Fig. 7. Aggregated LM of SG.

According to (3), (14), and (27)-(32), the transfer-function block diagram of the wind-thermal-bundled system is shown in Fig. 8.

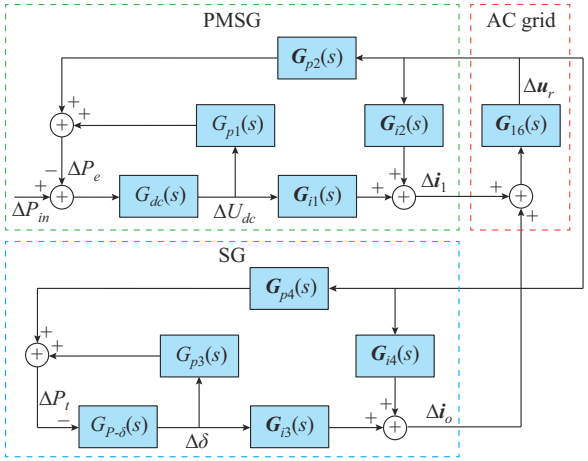

Fig. 8. Transfer-function block diagram of wind-thermal-bundled system.

From the above derivation, it is clear that the transfer-function block diagram of the system before and after the polymerization corresponds to each other, and the dynamic interaction analysis can be performed based on the transfer-function block diagram.

E. Validation of LM

Before analyzing the dynamic interaction mechanism, the accuracy of the LM in MATLAB should be validated using the ETM in DIgSILENT/PowerFactory. The reference DC voltage U_{dcref} has a step change from 1.1 p.u. to 1.05 p.u. at $t=1$ s, and the response curves of the system under LM and ETM are shown in Fig. 9. In Fig. 9, it is shown that the LM response is consistent with the ETM response, which verifies the correctness of the LM.

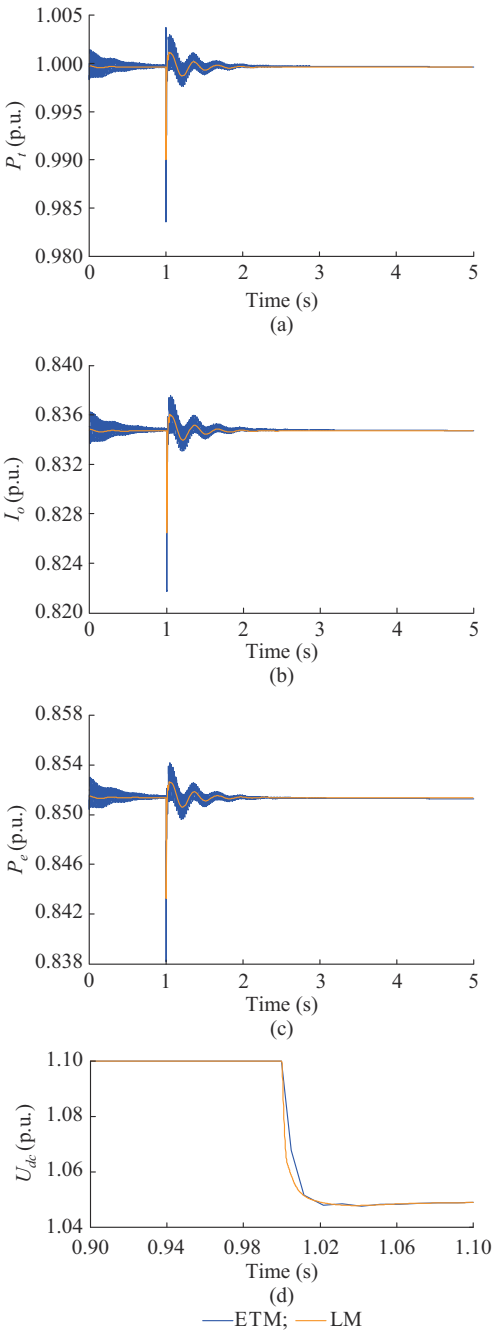

Fig. 9. Response curves following a change of U_{dcref} from 1.1 p.u. to 1.05 p.u.. (a) P_t of SG. (b) I_o of SG. (c) P_e of GSC. (d) U_{dc} of PMSG.

III. Damping Characteristic Analysis Based on PAM

In this section, the analysis of the damping path is presented based on the transfer-function block diagram. The block diagram is reconstructed to isolate the interaction damping. The factors influencing the damping characteristics are studied based on the damping reconstruction.

A. Damping Path Analysis

The block diagram of the damping path analysis, as shown in Fig. 10, clearly illustrates the relationship between each state variable and the corresponding link. This is beneficial for separating the disturbance transfer paths within the system. In the transfer function block diagram, the closed loop passing through the transfer function $G_{dc}(s)$ is defined as the SSO damping path. In Fig. 10, there are two damping paths which are represented by red and purple solid ovals, respectively, and the arrows indicate the direction of the disturbance transfer.

Damping path 1 can be described as the path through which the disturbance is transmitted from ΔU_{dc} to ΔP_e, assuming that ΔP_{in} remains constant.

Damping path 1 consists of the transfer functions $G_{dc}(s)$ and $G_{p1}(s)$. This indicates that path 1 is related to the DC capacitance of the PMSG and the outer loop control of the GSC. Damping path 1 is referred to as the internal oscillation transfer path of the PMSG.

Damping path 2 can be described as follows. When ΔP_e changes, the disturbance is transmitted from ΔU_{dc} to $\Delta \boldsymbol{i}_1$, then from $\Delta \boldsymbol{i}_1$ to $\Delta \boldsymbol{u}_r$, and finally from $\Delta \boldsymbol{u}_r$ to ΔP_e. Damping path 2 passes through three subsystems: PMSG, SG, and AC grid, and includes two closed-loop paths denoted as *a* and *b*, which are indicated by oval dashed lines. The closed-loop path *a* passes through $\Delta \boldsymbol{i}_1$ and $\Delta \boldsymbol{u}_r$, and consists of the trans-

fer function matrices $\boldsymbol{G}_{i2}(s)$ and $\boldsymbol{G}_{16}(s)$, which represent the interaction between the PMSG and the AC grid. The closed loop path *b* passes through $\Delta\boldsymbol{i}_o$ and $\Delta\boldsymbol{u}_r$ and consists of the transfer function matrices $\boldsymbol{G}_{i4}(s)$ and $\boldsymbol{G}_{16}(s)$, reflecting the interaction between the AC system and the SG. The closed loops *a* and *b* interact at the PCC voltage $\Delta\boldsymbol{u}_r$ to form a closed crossed loop. When the voltage $\Delta\boldsymbol{u}_r$ is disturbed, the currents $\Delta\boldsymbol{i}_1$ and $\Delta\boldsymbol{i}_o$ change due to the existence of closed loops *a* and *b*, which in turn affect the dynamics of $\Delta\boldsymbol{u}_r$. Thus, damping path 2 is referred to as the oscillation coupling path among the PMSG, SG, and AC grid.

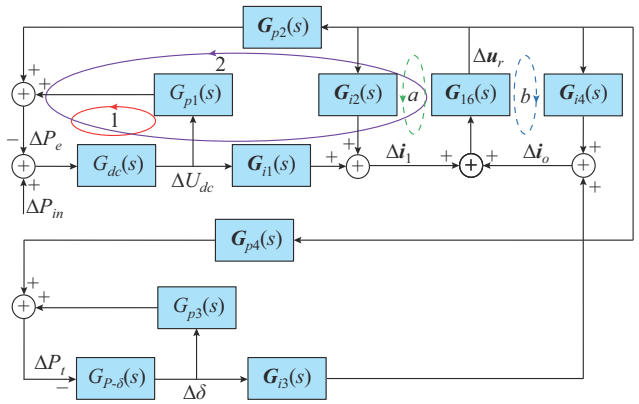

Fig. 10. Block diagram of damping path analysis.

Furthermore, the interaction processes can be divided into two groups: the controller interaction in the PMSG, and the interaction among the PMSG, SG, and AC grid. The controller interaction in the PMSG can be understood as the dynamic process of controller interaction in the PMSG system, which is caused by disturbances through a closed loop (damping path 1). The interaction between the PMSG, the SG, and the AC grid can be understood as the dynamic interplay between the subsystems triggered by voltage and current disturbances at the PCC driven by the closed loop (damping path 2).

B. Damping Separation Method

According to the superposition principle of linear systems, the transfer function block diagram is reconstructed, and the damping provided by the dynamic interaction is quantified. The damping separation procedure is as follows.

Step 1: based on (14) and (30), we can obtain (33) and Fig. 11(a).

$$\Delta\delta = \boldsymbol{G}_m(s)\begin{bmatrix}\Delta u_{rx}\\ \Delta u_{ry}\end{bmatrix} \tag{33}$$

where $\boldsymbol{G}_m(s)$ is the transfer function matrix from $\Delta\boldsymbol{u}_r$ to $\Delta\delta$. The expression of $\boldsymbol{G}_m(s)$ is given in (A16) in Appendix A.

Step 2: combining (28) and (21), we obtain (34) and Fig. 11(b).

$$\begin{bmatrix}\Delta i_{ox}\\ \Delta i_{oy}\end{bmatrix} = \boldsymbol{G}_n(s)\begin{bmatrix}\Delta u_{rx}\\ \Delta u_{ry}\end{bmatrix} \tag{34}$$

where $\boldsymbol{G}_n(s)$ is the transfer function matrix from $\Delta\boldsymbol{u}_r$ to $\Delta\boldsymbol{i}_o$. The expression of $\boldsymbol{G}_n(s)$ is given in (A17) in Appendix A.

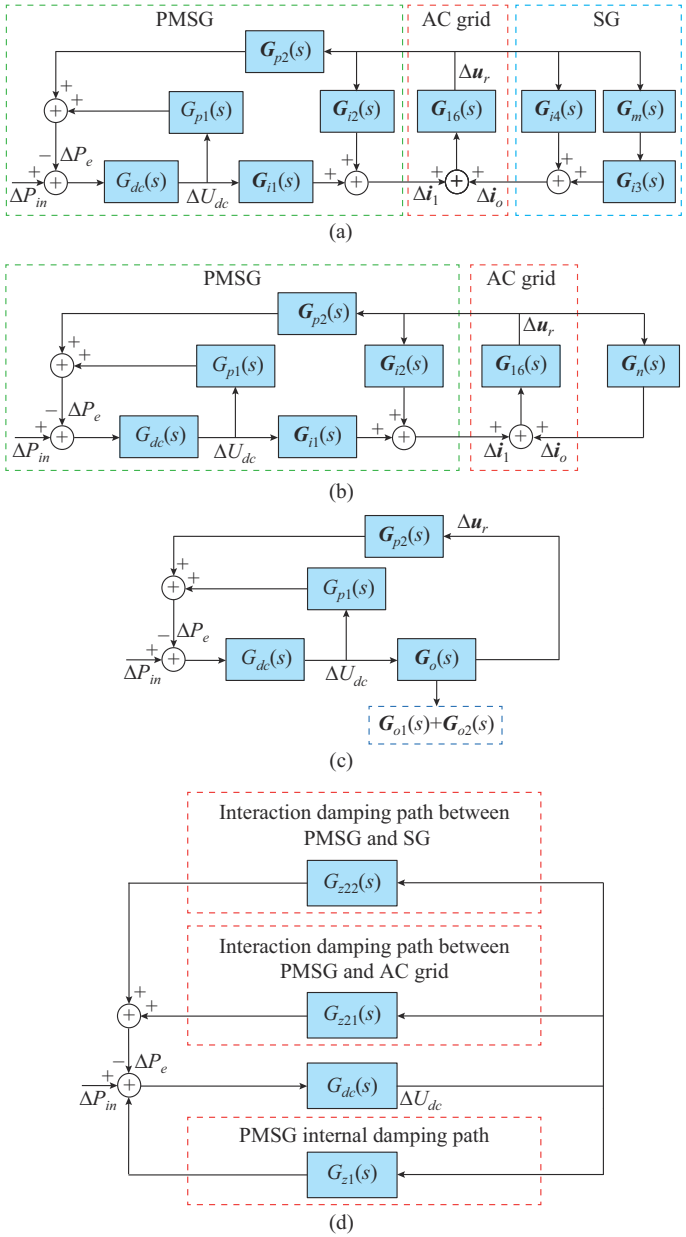

Fig. 11. Damping reconstruction process. (a) *Step 1*. (b) *Step 2*. (c) *Step 3*. (d) *Step 4*.

Step 3: combining (27), (29), and (34), we obtain (35) and Fig. 11(c).

$$\begin{bmatrix}\Delta u_{rx}\\ \Delta u_{ry}\end{bmatrix} = \boldsymbol{G}_o(s)\Delta U_{dc} \tag{35}$$

where $\boldsymbol{G}_o(s)$ is the transfer function matrix from ΔU_{dc} to $\Delta\boldsymbol{u}_r$.

The open-loop transfer function matrix $\boldsymbol{G}_o(s)$ represents the interaction between the PMSG and the SG and the interaction between the PMSG and the AC system. If $\Delta\boldsymbol{i}_o = \boldsymbol{0}$, i.e., the SG is not connected to the system and the interaction between the PMSG and the SG is not considered, the block diagram is simplified. The corresponding open loop transfer function matrix $\boldsymbol{G}_{o1}(s)$ is obtained by substituting (29) into (27). $\boldsymbol{G}_{o1}(s)$ represents the interaction between the PMSG and the AC grid. According to the superposition prin-

ciple of linear systems, $\boldsymbol{G}_o(s)$ is subtracted from $\boldsymbol{G}_{o1}(s)$ to obtain $\boldsymbol{G}_{o2}(s)$, where $\boldsymbol{G}_{o2}(s)$ represents the interaction between the PMSG and the SG. The expressions for $\boldsymbol{G}_o(s)$, $\boldsymbol{G}_{o1}(s)$, and $\boldsymbol{G}_{o2}(s)$ are given in (36), and the transfer function block diagram is shown in Fig. 11(c).

$$\begin{cases} \boldsymbol{G}_o(s) = \left(\boldsymbol{I} - \boldsymbol{G}_{16}(s)\left(\boldsymbol{G}_{i2}(s) + \boldsymbol{G}_n(s)\right)\right)^{-1} \boldsymbol{G}_{16}(s) G_{i1}(s) \\ \boldsymbol{G}_{o1}(s) = \left(\boldsymbol{I} - \boldsymbol{G}_{16}(s)\boldsymbol{G}_{i2}(s)\right)^{-1} \boldsymbol{G}_{16}(s) G_{i1}(s) \\ \boldsymbol{G}_{o2}(s) = \boldsymbol{G}_o(s) - \boldsymbol{G}_{o1}(s) \end{cases} \tag{36}$$

Step 4: when ΔP_{in} is selected as the input variable and ΔU_{dc} is selected as the output variable, three transfer functions from ΔU_{dc} to the variables ΔP_e-ΔP_{in} and ΔP_e are obtained using the damping separation method, as shown in Fig. 11(d) and (37).

$$\begin{cases} G_{z1}(s) = G_{p1}(s) \\ G_{z21}(s) = \boldsymbol{G}_{p2}(s)\boldsymbol{G}_{o1}(s) \\ G_{z22}(s) = \boldsymbol{G}_{p2}(s)\boldsymbol{G}_{o2}(s) \end{cases} \tag{37}$$

where $G_{z1}(s)$ is the internal damping of the PMSG; $G_{z21}(s)$ is the damping of the DC capacitance oscillation influenced by the interaction between the PMSG and the AC grid; and $G_{z22}(s)$ is the damping influenced by the interaction between the PMSG and the SG system.

The corresponding damping coefficient can be calculated from:

$$\begin{cases} Z_1 = \mathrm{Im}\left(\mathrm{j}\omega_d G_{z1}(\mathrm{j}\omega_d)\right)/\omega_d \\ Z_{21} = \mathrm{Im}\left(\mathrm{j}\omega_d G_{z21}(\mathrm{j}\omega_d)\right)/\omega_d \\ Z_{22} = \mathrm{Im}\left(\mathrm{j}\omega_d G_{z22}(\mathrm{j}\omega_d)\right)/\omega_d \\ Z_2 = Z_{21} + Z_{22} \end{cases} \tag{38}$$

where Z_1 is the PMSG self-damping coefficient; Z_{21} is the PMSG-grid interaction damping coefficient; Z_{22} is the PMSG-SG interaction damping coefficient; and Z_2 is the interaction damping coefficient. The total damping coefficient of the system is $Z = Z_1 + Z_2$.

C. Analysis of Influence Factors

1) Proportional Coefficient of DC Voltage Outer Loop of GSC

To study the influence of the proportional coefficient of DC voltage outer loop of GSC control K_{pdc} on the damping coefficient, Fig. 12(a) shows the frequency characteristic curves of damping coefficients Z_{21} and Z_{22} at different K_{pdc}. Figure 12(b) shows the frequency characteristic curves of self-damping coefficient Z_1, interaction damping coefficient Z_2, and total damping coefficient Z at different K_{pdc}. The values of K_{pdc} are 12, 18, and 25, respectively. The arrow indicates the change direction of the frequency characteristic curves with increasing K_{pdc}.

As shown in Fig. 12(a), as K_{pdc} increases, the interaction damping between the PMSG and the SG increases, and the interaction damping between the PMSG and the AC grid decreases. As shown in Fig. 12(b), as K_{pdc} increases, the frequency characteristic curves of Z_1, Z_2, and Z move upward, indicating that the increase in K_{pdc} causes the self-damping coefficient Z_1, the interaction damping coefficient Z_2, and the total damping coefficient Z to increase.

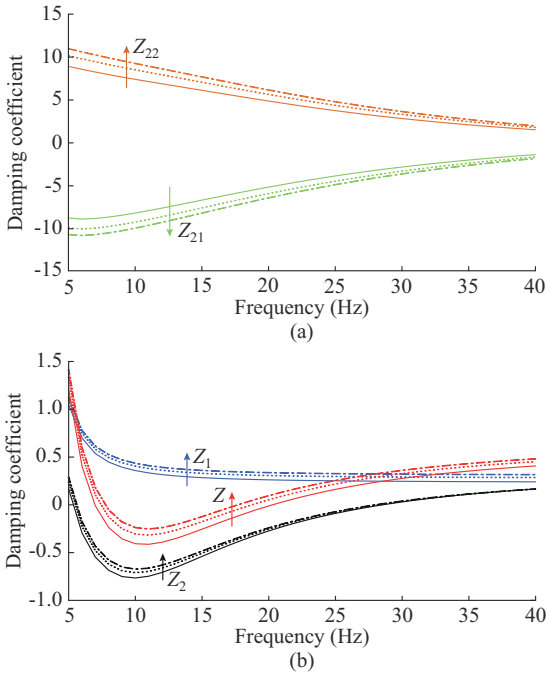

Fig. 12. Damping characteristic analysis with change of K_{pdc}. (a) Frequency characteristic curves of Z_{21} and Z_{22}. (b) Frequency characteristic curves of Z_1, Z_2, and Z.

2) Integral Coefficient of DC Voltage Outer Loop of GSC

To study the influence of the integral coefficient of DC voltage outer loop of GSC control K_{idc} on the damping coefficient, Fig. 13(a) shows the frequency characteristic curves of damping coefficients Z_{21} and Z_{22} at different K_{idc}. Figure 13 (b) shows the frequency characteristic curves of self-damping coefficient Z_1, interaction damping coefficient Z_2, and total damping coefficient Z at different K_{idc}. The values of K_{idc} are 133, 233, and 333, respectively. The arrow indicates the change direction of the frequency characteristic curves as K_{idc} increases.

As shown in Fig. 13(a), as K_{idc} increases, the interaction damping coefficient between the PMSG and the SG increases, and the interaction damping coefficient between the PMSG and the AC grid decreases. As shown in Fig. 13(b), as K_{idc} increases, the frequency characteristic curve of Z_1 moves upward, indicating that the positive damping effect provided by the PMSG increases. The frequency characteristic curve of Z_2 moves downward, indicating that the interaction damping decreases. The total damping coefficient Z decreases and the system stability is weakened.

3) Grid Strength

To study the influence of short-circuit ratio (SCR) on the damping coefficient, Fig. 14(a) shows the frequency characteristic curves of damping coefficients Z_{21} and Z_{22} under different SCRs. Figure 14(b) shows the frequency characteristic curves of self-damping coefficient Z_1, interaction damping coefficient Z_2, and total damping coefficient Z under different SCR. The values of SCR are 1, 2, and 3, respectively. The arrow indicates the change direction of the frequency characteristic curves as the SCR increases.

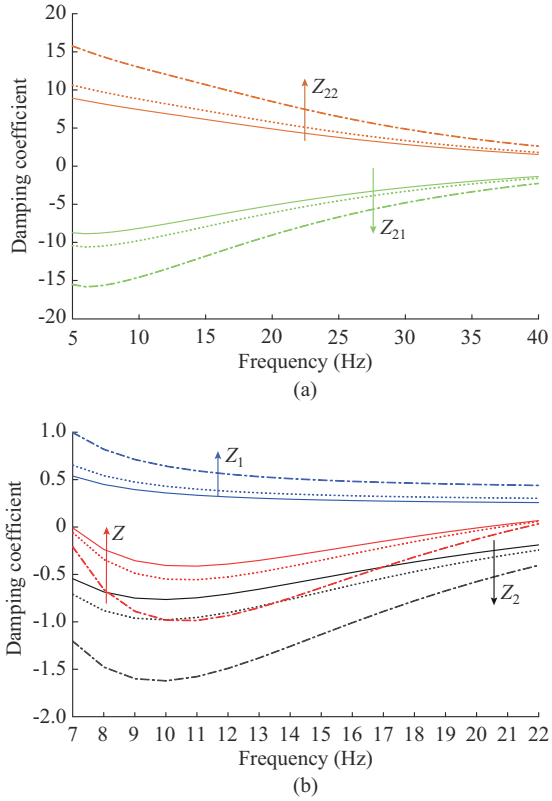

Fig. 13. Damping characteristic analysis with change of K_{idc}. (a) Frequency characteristic curves of Z_{21} and Z_{22}. (b) Frequency characteristic curves of Z_1, Z_2, and Z.

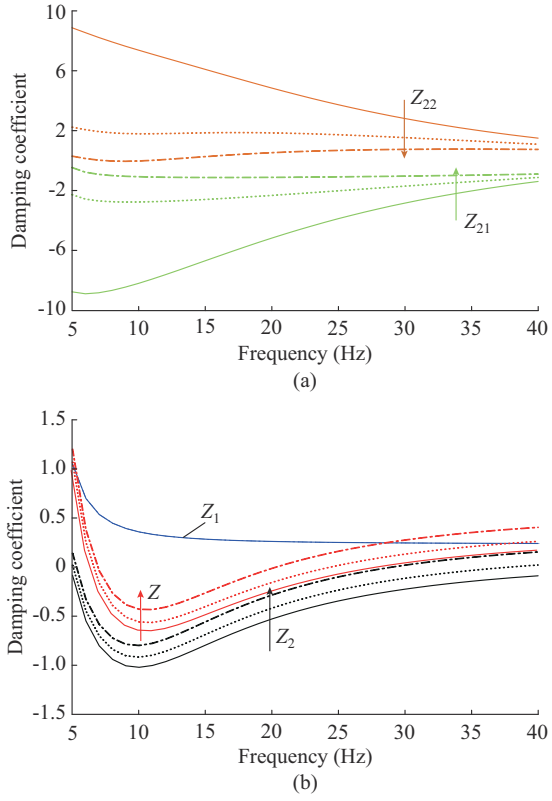

Fig. 14. Damping characteristic analysis with change of SCR. (a) Frequency characteristic curves of Z_{21} and Z_{22}. (b) Frequency characteristic curves of Z_1, Z_2, and Z.

As shown in Fig. 14(a), as the SCR increases, the interaction damping between the PMSG and the SG decreases, and the interaction damping between the PMSG and the AC power grid increases. As shown in Fig. 14(b), the frequency characteristic curve of Z_1 remains unchanged as the SCR increases, indicating that the positive damping effect provided by the PMSG is independent of the power system strength. The frequency characteristic curves of Z_2 and Z move upward, indicating that the interaction damping and the total damping increase.

4) Time Constant of Hydraulic Motor T_1

To study the influence of the time constant of the hydraulic motor T_1 on the damping coefficient, Fig. 15(a) shows the frequency characteristic curves of damping coefficients Z_{21} and Z_{22} under different T_1. Figure 15(b) shows the frequency characteristic curves of self-damping coefficient Z_1, interaction damping coefficient Z_2, and total damping coefficient Z under different T_1. The values of T_1 are 0.5, 2, and 5, respectively. The arrow indicates the change direction of the frequency characteristic curves as T_1 increases.

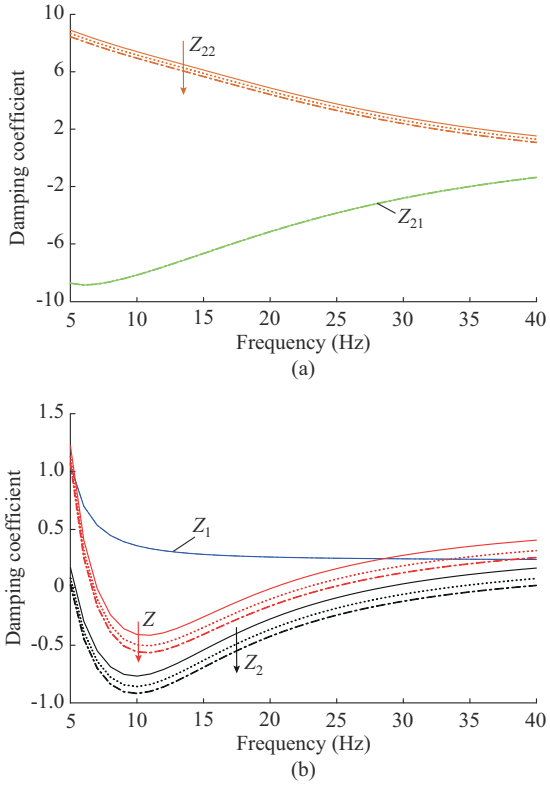

Fig. 15. Damping characteristic analysis with change of T_1. (a) Frequency characteristic curves of Z_{21} and Z_{22}. (b) Frequency characteristic curves of Z_1, Z_2, and Z.

As shown in Fig. 15(a), as T_1 increases, the interaction damping between the PMSG and the SG decreases, and the interaction damping between the PMSG and the AC grid remains unchanged. As shown in Fig. 15(b), the frequency characteristic curve of Z_1 remains unchanged as T_1 increases. The frequency characteristic curves of Z_2 and Z move downward, indicating that the interaction damping and the total damping decrease.

IV. Damping Characteristic Analysis Based on Eigenvalue Analysis Method

A. Eigenvalue Analysis

The small-signal models for PMSG and SG have been extensively studied, e.g., [31]-[33], and will not be discussed here. The state space model for the system is given as:

$$\frac{\mathrm{d}\Delta \boldsymbol{X}}{\mathrm{d}t} = \boldsymbol{A}\Delta \boldsymbol{X} + \boldsymbol{B}\Delta \boldsymbol{u} \tag{39}$$

Based on (37) and the parameters in Appendix B Table BI, the primary oscillation modes of the wind-thermal-bundled system are shown in Table I.

TABLE I
Oscillation Modes of Wind-Thermal-Bundled System

Oscillation mode	Eigenvalue	Oscillation frequency (Hz)	Damping ratio
$\lambda_{1,2}$	$-3.35 \pm j15.870$	2.53	0.2063
$\lambda_{3,4}$	$20.77 \pm j53.460$	8.51	–0.3621
$\lambda_{5,6}$	$-10.50 \pm j90.670$	14.43	0.1150
$\lambda_{7,8}$	$-12.59 \pm j321.130$	51.11	0.0392
$\lambda_{9,10}$	$-22.53 \pm j356.598$	56.75	0.0631
$\lambda_{11,12}$	$-66.48 \pm j1799.400$	286.39	0.0369

As shown in Table I, the system has six oscillation modes: one LFO mode $\lambda_{1,2}$, two SSO modes $\lambda_{3,4}$, $\lambda_{5,6}$, and three medium-high frequency oscillation modes $\lambda_{7,8}$, $\lambda_{9,10}$, and $\lambda_{11,12}$. The real parts of modes $\lambda_{1,2}$, $\lambda_{5,6}$, $\lambda_{7,8}$, $\lambda_{9,10}$, and $\lambda_{11,12}$ are negative, i.e., these modes are stable oscillation modes. The real part of the mode $\lambda_{3,4}$ is positive, i.e., mode 5 is an unstable SSO mode.

The normalized PFs of the oscillation modes have been calculated, and it has been shown that the oscillation mode $\lambda_{3,4}$ is associated with the DC voltage control of the GSC. The effect of the system parameters on the mode $\lambda_{3,4}$ is studied.

B. Influence of Parameters on Oscillation Mode

1) Proportional Coefficient of DC Voltage Outer Loop of GSC

Figure 16 shows the variation of the oscillation mode $\lambda_{3,4}$ and the damping ratio as K_{pdc} changes from 4 to 16. In Fig. 16, the arrows indicate the variation of $\lambda_{3,4}$ and damping ratio as K_{pdc} increases.

As shown in Fig. 16, the increase in K_{pdc} causes the oscillation mode $\lambda_{3,4}$ to shift to the left, resulting in an increase in the damping ratio and indicating improved stability.

2) Integral Coefficient of DC Voltage Outer Loop of GSC

Figure 17 shows the variation of the oscillation mode $\lambda_{3,4}$ and the damping ratio as K_{idc} changes from 40 to 120. In Fig. 17, the arrows indicate the variation of $\lambda_{3,4}$ and damping ratio as K_{idc} increases.

Figure 17 shows that as K_{idc} increases, $\lambda_{3,4}$ moves to the right and the damping ratio decreases, indicating a gradual destabilization of the system.

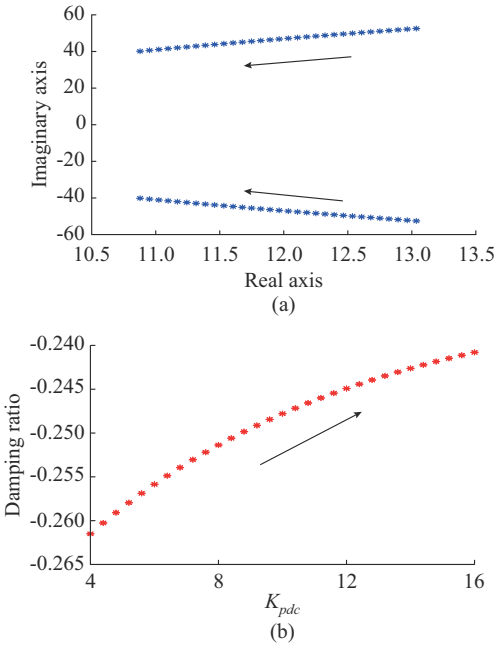

Fig. 16. Variation of oscillation mode $\lambda_{3,4}$ and damping ratio with different K_{pdc}. (a) Oscillation mode. (b) Damping ratio.

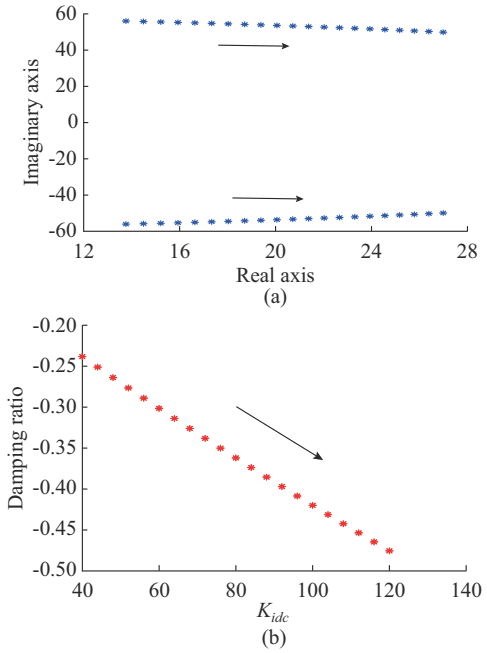

Fig. 17. Variation of oscillation mode $\lambda_{3,4}$ and damping ratio with different K_{idc}. (a) Oscillation mode. (b) Damping ratio.

V. Simulation Results

In this section, the wind-thermal-bundled system is constructed in DIgSILENT. At $t=1$ s, K_{idc} is changed from 133 to 1000 to excite SSO. Other parameters are in accordance with Appendix B Table BI. The DC capacitance voltage curves with different parameters are shown to validate the above analysis. When the system is disturbed, the DC voltage curves with different K_{pdc}, K_{idc}, SCR, and T_1 are shown in Fig. 18.

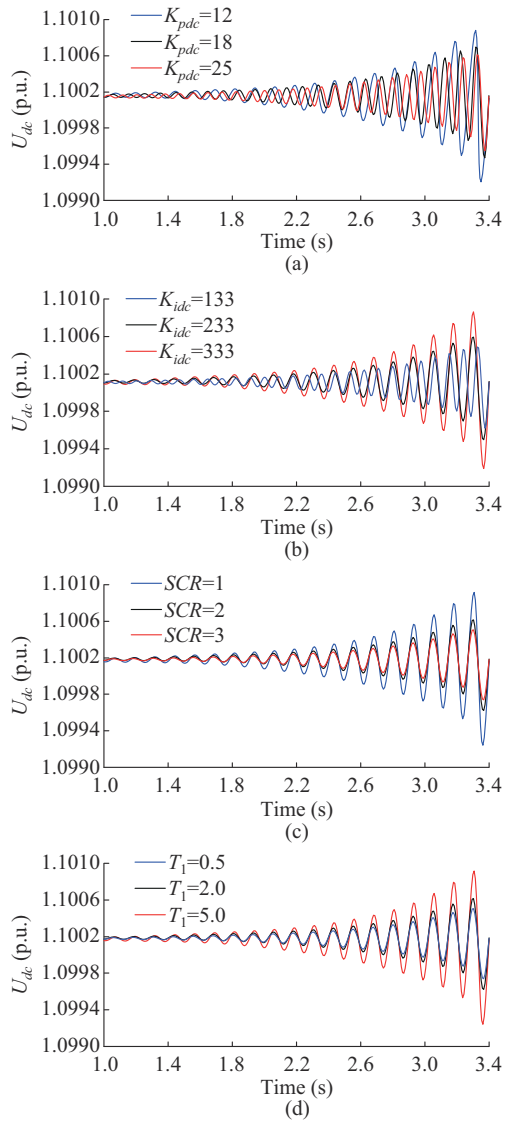

Fig. 18. DC voltage response curves with different parameters. (a) K_{pdc}. (b) K_{idc}. (c) SCR. (d) T_1.

In Fig. 18, it can be observed that the DC voltage fluctuation decreases as K_{pdc} or SCR increases. The DC voltage fluctuation increases as K_{idc} or T_1 increases. The results of the damping characteristics analysis are validated by time-domain simulations.

VI. Conclusion

The damping characteristics of the wind-thermal-bundled system are analyzed using the PAM. The conclusions are given as follows.

1) The LMs for the PMSG, SG, and AC grid are established, respectively, and the LMs of the subsystems are connected to construct the transfer-function block diagram of the system.

2) The damping path analysis is presented based on the transfer-function block diagram. The interaction mechanism between the subsystems can be interpreted as a dynamic process driven by voltage disturbances and current disturbances at the PCC.

3) Based on the damping separation, the total damping of the DC capacitance-dominated oscillation mode can be divided into three parts: PMSG internal damping coefficient, PMSG-SG interaction damping coefficient, and PMSG-grid interaction damping coefficient.

4) The effect of the parameters on the damping characteristics is analyzed using the damping separation method and the eigenvalue analysis method, respectively. The analysis shows that K_{pdc} and SCR have a positive effect on the damping of the DC capacitance-dominated oscillation mode, while K_{idc} and T_1 have a negative effect. The analysis results are of great importance for practical engineering.

Appendix A

$\boldsymbol{G}_1$ in (2) is given as:

$$\boldsymbol{G}_1(s) = \begin{bmatrix} 1.5u_{td0} & 1.5i_{gd0} \end{bmatrix} \tag{A1}$$

$\boldsymbol{G}_2$ in (6) is given as:

$$\boldsymbol{G}_2(s) = \begin{bmatrix} sL_g & 1 \end{bmatrix} \tag{A2}$$

$\boldsymbol{G}_3(s)$ and $\boldsymbol{G}_4(s)$ in (7) and (8) are given as:

$$\begin{cases} \boldsymbol{G}_3(s) = -\boldsymbol{G}_4(s) = \begin{bmatrix} G_{C1}(s) & G_{C2}(s) \\ -G_{C2}(s) & G_{C1}(s) \end{bmatrix} \\ G_{C1}(s) = \dfrac{1}{C_1\left(s + \omega_0^2/s\right)} \\ G_{C2}(s) = \dfrac{\omega_0 G_{C1}(s)}{s} \end{cases} \tag{A3}$$

$$\begin{cases} \boldsymbol{G}_5(s) = -\boldsymbol{G}_6(s) = \begin{bmatrix} G_{L1}(s) & G_{L2}(s) \\ -G_{L2}(s) & G_{L1}(s) \end{bmatrix} \\ G_{L1}(s) = \dfrac{R_1 + sL_1}{L_1^2 s^2 + L_1^2\omega_0^2 + 2sL_1R_1 + R_1^2} \\ G_{L2}(s) = \dfrac{\omega_0 L_1}{L_1^2 s^2 + L_1^2\omega_0^2 + 2sL_1R_1 + R_1^2} \end{cases} \tag{A4}$$

$\boldsymbol{T}_{ug}$ and $\boldsymbol{T}_{ig}$ in (9) and (10) are given as:

$$\begin{cases} \boldsymbol{T}_{ug} = \begin{bmatrix} \cos\theta_{PLL0} & \sin\theta_{PLL0} & k_1 \\ -\sin\theta_{PLL0} & \cos\theta_{PLL0} & k_2 \end{bmatrix} \\ \boldsymbol{T}_{ig} = \begin{bmatrix} \cos\theta_{PLL0} & -\sin\theta_{PLL0} & k_3 \\ \sin\theta_{PLL0} & \cos\theta_{PLL0} & k_4 \end{bmatrix} \end{cases} \tag{A5}$$

$$\begin{cases} k_1 = -u_{gx0}\sin\theta_{PLL0} + u_{gy0}\cos\theta_{PLL0} \\ k_2 = -u_{gx0}\cos\theta_{PLL0} - u_{gy0}\sin\theta_{PLL0} \\ k_3 = -i_{gd0}\sin\theta_{PLL0} - i_{gq0}\cos\theta_{PLL0} \\ k_4 = i_{gd0}\cos\theta_{PLL0} - i_{gq0}\sin\theta_{PLL0} \end{cases} \tag{A6}$$

$\boldsymbol{G}_9(s)$ in (17) is given as:

$$\begin{cases} \boldsymbol{G}_9(s) = \begin{bmatrix} a_{9\_1} & a_{9\_2} \end{bmatrix} \\ a_{9\_1} = \left[T'_{d0}s + 1 + \left(X_d - X'_d\right)a_{12}\right]^{-1}\left(X_d - X'_d\right)a_{11} \\ a_{9\_2} = \left[T'_{d0}s + 1 + \left(X_d - X'_d\right)a_{12}\right]^{-1}\left(X_d - X'_d\right)a_{12} \\ \begin{bmatrix} a_{11} & a_{12} \\ a_{21} & a_{22} \end{bmatrix} = \begin{bmatrix} -R - R_o - sL_o & -X'_q + \omega_g L_o \\ X'_d - \omega_g L_o & -R - R_o - sL_o \end{bmatrix}^{-1} \end{cases} \tag{A7}$$

$\boldsymbol{G}_{10}(s)$ in (18) is given as:

$$\begin{cases} \boldsymbol{G}_{10}(s)=\begin{bmatrix} a_{10\_1} & a_{10\_2} \\ a_{10\_3} & a_{10\_4} \end{bmatrix} \\ a_{10\_1}=a_{11}+a_{12}a_{9\_1} \\ a_{10\_2}=a_{12}+a_{12}a_{9\_2} \\ a_{10\_3}=a_{21}+a_{22}a_{9\_1} \\ a_{10\_4}=a_{22}+a_{22}a_{9\_2} \end{cases} \tag{A8}$$

$\boldsymbol{G}_{12}$ and $\boldsymbol{G}_{13}$ in (21) and (22) are given as:

$$\begin{cases} \boldsymbol{G}_{12}=\begin{bmatrix} \cos\delta_0 & \sin\delta_0 & k_5 \\ -\sin\delta_0 & \cos\delta_0 & k_6 \end{bmatrix} \\ \boldsymbol{G}_{13}=\begin{bmatrix} \cos\delta_0 & -\sin\delta_0 & k_7 \\ \sin\delta_0 & \cos\delta_0 & k_8 \end{bmatrix} \end{cases} \tag{A9}$$

$$\begin{cases} k_5=-u_{rx0}\sin\delta_0+u_{ry0}\cos\delta_0 \\ k_6=-u_{rx0}\cos\delta_0-u_{ry0}\sin\delta_0 \\ k_7=-i_{od20}\sin\delta_0-i_{oq20}\cos\delta_0 \\ k_8=i_{od20}\cos\delta_0-i_{oq20}\sin\delta_0 \end{cases} \tag{A10}$$

$\boldsymbol{G}_{14}(s)$ and $\boldsymbol{G}_{15}(s)$ in (23) are given as:

$$\begin{cases} \boldsymbol{G}_{14}(s)=-\boldsymbol{G}_{15}(s)=\begin{bmatrix} G_{L5}(s) & G_{L6}(s) \\ -G_{L6}(s) & G_{L5}(s) \end{bmatrix} \\ G_{L5}(s)=\dfrac{R_2+sL_2}{L_2^2s^2+L_2^2\omega_0^2+2sL_2R_2+R_2^2} \\ G_{L6}(s)=\dfrac{\omega_0 L_2}{L_2^2s^2+L_2^2\omega_0^2+2sL_2R_2+R_2^2} \end{cases} \tag{A11}$$

$\boldsymbol{G}_{16}(s)$ in (26) is given as:

$$\boldsymbol{G}_{16}(s)=\boldsymbol{G}_{14}^{-1}(s) \tag{A12}$$

$G_{p3}(s)$ and $\boldsymbol{G}_{p4}(s)$ in (29) are given as:

$$\begin{cases} G_{p3}(s)=a_{11\_1}k_5+a_{11\_2}k_6 \\ \boldsymbol{G}_{p4}(s)=\begin{bmatrix} a_{p4\_1} & a_{p4\_2} \end{bmatrix} \\ a_{p4\_1}=a_{11\_1}\cos\delta_0-a_{11\_2}\sin\delta_0 \\ a_{p4\_2}=a_{11\_1}\sin\delta_0+a_{11\_2}\cos\delta_0 \end{cases} \tag{A13}$$

where $a_{11\_1}=\boldsymbol{G}_{11}(1,1)$; and $a_{11\_2}=\boldsymbol{G}_{11}(1,2)$.

$\boldsymbol{G}_{i3}(s)$ and $\boldsymbol{G}_{i4}(s)$ in (30) are given as:

$$\begin{cases} \boldsymbol{G}_{i3}(s)=\begin{bmatrix} a_{i3\_1} \\ a_{i3\_2} \end{bmatrix} \\ \boldsymbol{G}_{i4}(s)=\begin{bmatrix} a_{i4\_1} & a_{i4\_2} \\ a_{i4\_3} & a_{i4\_4} \end{bmatrix} \end{cases} \tag{A14}$$

$$\begin{cases} a_{i3\_1}=-\sin\delta_0 a_{10\_2}k_5+\cos\delta_0 a_{10\_1}k_6+k_7 \\ a_{i3\_2}=\cos\delta_0 a_{10\_2}k_5+\sin\delta_0 a_{10\_1}k_6+k_8 \\ a_{i4\_1}=-\sin\delta_0\cos\delta_0\left(a_{10\_1}+a_{10\_2}\right) \\ a_{i4\_2}=-\left(\sin\delta_0\right)^2 a_{10\_2}+\left(\cos\delta_0\right)^2 a_{10\_1} \\ a_{i4\_3}=\left(\cos\delta_0\right)^2 a_{10\_2}-\left(\sin\delta_0\right)^2 a_{10\_1} \\ a_{i4\_4}=\sin\delta_0\cos\delta_0\left(a_{10\_1}+a_{10\_2}\right) \end{cases} \tag{A15}$$

$\boldsymbol{G}_m(s)$ in (31) is given as:

$$\boldsymbol{G}_m(s)=-\left(1+G_{p\text{-}\delta}(s)G_{p3}(s)\right)^{-1}\boldsymbol{G}_{p4}(s) \tag{A16}$$

$\boldsymbol{G}_n(s)$ in (32) is given as:

$$\boldsymbol{G}_n(s)=\boldsymbol{G}_{i3}(s)\boldsymbol{G}_m(s)+\boldsymbol{G}_{i4}(s) \tag{A17}$$

APPENDIX B

TABLE BI
PARAMETERS OF WIND-THERMAL-BUNDLED SYSTEM

Module	Parameter	Value
PMSG	Rated power P_n (MW)	275
	DC capacitance C_{dc} (mF)	2
	Filter inductance L_g (H)	0.003
	Filter resistance R_g (Ω)	0.03
	Line resistance R_1 (Ω)	0.02
	Line inductance L_1(H)	0.002
	Line capacitance C_1 (μF)	5
GSC	Outer loop proportional coefficient K_{pdc}	18
	Outer loop integral coefficient K_{idc}	133
	Inner loop proportional coefficient K_{p1}	45
	Inner loop integral coefficient K_{i1}	2
PLL	Proportional coefficient k_{pPLL}	10
	Integral coefficient k_{iPLL}	30
SG	Resistance R (p.u.)	0.1
	d-axis reactance X_d (p.u.)	1.59
	q-axis transient reactance X'_q (p.u.)	0.46
	d-axis transient reactance X'_d (p.u.)	0.25
	Line resistance R_o (Ω)	0.03
	Line inductance L_o (H)	0.001
	d-axis transient time constant T'_d (s)	0.68
	Inertia M	1.759
Turbine	Time constant of steam volume T_{CH}	0.5
	Time constant of reheater T_{RH}	8
	Time constant of cross-pipe T_{CO}	1
	Power proportional coefficients of high-pressure cylinder F_{HP}	0.3
	Power proportional coefficients of middle pressure cylinder F_{IP}	0.3
	Power proportional coefficients of low-pressure cylinder F_{LP}	0.4
Governor	Time constant of hydraulic motor T_1	0.5
	Amplification factor K_p	1
	Reciprocal of unequal rate K_δ	1
Exciter	Excitation regulation gain K_A	1
	Excitation regulation time constant T_A	0.2
AC grid	Equivalent resistance R_2 (Ω)	0.01
	Equivalent inductance L_2 (H)	0.1

REFERENCES

[1] M. Dicorato, G. Forte, M. Trovato *et al*., "Transmission system and offshore wind farms: challenges and chances," in *Proceedings of 2018 5th International Symposium on Environment-friendly Energies and Applications*, Rome, Italy, Sept. 2018, pp. 1-6.

[2] J. Yan, H. Lin, Y. Feng *et al*., "Improved sliding mode model reference adaptive system speed observer for fuzzy control of direct-drive permanent magnet synchronous generator wind power generation system," *IET Renewable Power Generation*, vol. 7, no. 1, pp. 28-35, Feb. 2013.

[3] R. Li, S. Zhao, B. Gao *et al*., "Sub-synchronous torsional interaction of steam turbine under wind power oscillation in wind-thermal bundled transmission systems," *International Journal of Electrical Power*

& Energy Systems, vol. 108, pp. 445-455, Jun. 2019.
[4] Q. Geng, H. Sun, X. Zhou *et al*., "A storage-based fixed-time frequency synchronization method for improving transient stability and resilience of smart grid," *IEEE Transactions on Smart Grid*, vol. 14, no. 6, pp. 4799-4815, Nov. 2023.
[5] Q. Geng, H. Sun, and X. Zhou, "Distributed fixed-time transient stability control scheme for power systems with heterogeneous dynamics," *IEEE Transactions on Power Systems*, vol. 39, no. 1, pp. 1693-1710, Jan. 2024.
[6] Q. Geng, H. Sun, X. Zhang *et al*., "Mitigation of oscillations in three phase LCL-filtered grid converters based on proportional resonance and improved model predictive control," *IEEE Transactions on Industry Applications*, vol. 59, no. 2, pp. 2590-2602, Mar.-Apr. 2023.
[7] K. Sun, W. Yao, J. Fang *et al*., "Impedance modeling and stability analysis of grid-connected DFIG-based wind farm with a VSC-HVDC," *IEEE Journal of Emerging and Selected Topics in Power Electronics*, vol. 8, no. 2, pp. 1375-1390, Jun. 2020.
[8] B. Shao, S. Zhao, B. Gao *et al*., "Adequacy of the single-generator equivalent model for stability analysis in wind farms with VSC-HVDC systems," *IEEE Transactions on Energy Conversion*, vol. 36, no. 2, pp. 907-918, Jun. 2021.
[9] W. Du, Q. Fu, and H. Wang, "Subsynchronous oscillations caused by open-loop modal coupling between VSC-Based HVDC line and power system," *IEEE Transactions on Power Systems*, vol. 33, no. 4, pp. 3664-3677, Jul. 2018.
[10] M. Liserre, R. Teodorescu, and F. Blaabjerg, "Stability of photovoltaic and wind turbine grid-connected inverters for a large set of grid impedance values," *IEEE Transactions on Power Electronics*, vol. 21, no. 1, pp. 263-272, Jan. 2006.
[11] E. Hagstrom, I. Norheim, and K. Uhlen, "Large-scale wind power integration in Norway and impact on damping in the Nordic grid," *Wind Energy*, vol. 8, no. 3, pp. 375-384, Jul.-Sept. 2005.
[12] T. Knüppel, J. N. Nielsen, K. H. Jensen *et al*., "Small-signal stability of wind power system with full-load converter interfaced wind turbine," *IET Renewable Power Generation*, vol. 6, no. 2, pp.79-91, Mar. 2012.
[13] K. M. Alawasa, A. R. I. Mohamed, and W. Xu, "Modeling, analysis, and suppression of the impact of full-scale wind-power converters on subsynchronous damping," *IEEE Systems Journal*, vol. 7, no. 4, pp. 700-712, Dec. 2013.
[14] J. Quintero, V. Vittal, G. T. Heydt *et al*., "The impact of increased penetration of converter control-based generators on power system modes of oscillation," *IEEE Transactions on Power Systems*, vol. 29, no. 5, pp. 2248-2256, Sept. 2014.
[15] W. Du, X. Chen, and H. Wang, "Power system electromechanical oscillation modes as affected by dynamic interactions from grid-connected PMSGs for wind power generation," *IEEE Transactions on Sustainable Energy*, vol. 8, no. 3, pp. 1301-1312, Jul. 2017.
[16] Y. Huang, X. Yuan, J. Hu *et al*., "DC-bus voltage control stability affected by AC-bus voltage control in VSCs connected to weak AC grids," *IEEE Journal of Emerging & Selected Topics in Power Electronics*, vol. 4, no. 2, pp. 445-458, Jun. 2016.
[17] W. Du, X. Chen, and H. Wang, "PLL-induced modal resonance of grid-connected PMSGs with the power system electromechanical oscillation modes," *IEEE Transactions on Sustainable Energy*, vol. 8, no. 4, pp. 1581-1591, Oct. 2017.
[18] H. Yuan, X. Yuan, and J. Hu, "Modeling of grid-connected VSCs for power system small-signal stability analysis in DC-link voltage control timescale," *IEEE Transactions on Power Systems*, vol. 32, no. 5, pp. 3981-3991, Sept. 2017.
[19] Y. Huang, X. Zhai, J. Hu *et al*., "Modeling and stability analysis of VSC internal voltage in DC-link voltage control timescale," *IEEE Journal of Emerging & Selected Topics in Power Electronics*, vol. 6, no. 1, pp. 16-28, Mar. 2018.
[20] L. Zheng and S. Ma, "DC-bus voltage damping characteristic analysis and optimization of grid-connected PMSG," *Electric Power Systems Research*, vol. 216, pp. 108980-108989, Mar. 2023.
[21] D. Lu, X. Wang, and F. Blaabjerg, "Impedance-based analysis of DC link voltage dynamics in voltage-source converters," *IEEE Transactions on Power Electronics*, vol. 34, no. 4, pp. 3973-3985, Apr. 2019.
[22] D. Wang, L. Liang, L. Shi *et al*., "Analysis of modal resonance between PLL and DC-link voltage control in weak-grid tied VSCs," *IEEE Transactions on Power Systems*, vol. 34, no. 2, pp. 1127-1138, Mar. 2019.
[23] G. O. Kalcon, G. P. Adam, O. Anaya-Lara *et al*., "Small signal stability analysis of multi-terminal VSC-based DC transmission systems," *IEEE Transactions on Power Systems*, vol. 27, no. 4, pp.1818-1830, Nov. 2012.
[24] J. Hu, Y. Huang, D. Wang *et al*., "Modeling of grid connected DFIG-based wind turbines for DC-link voltage stability analysis," *IEEE Transactions on Sustainable Energy*, vol. 6, no. 4, pp. 1325-1336, Oct. 2015.
[25] Y. Huang, X. Yuan, J. Hu *et al*., "Modeling of VSC connected to weak grid for stability analysis of DC-link voltage control," *IEEE Journal of Emerging & Selected Topics in Power Electronics*, vol. 3, no. 3, pp. 1193-1204, Dec. 2015.
[26] B. Gao, Y. Wang, S. Zeng *et al*., "Analysis of sub-synchronous component path and damping characteristics of D-PMSG-based wind farm incorporated into weak AC grid," *Proceedings of the CSEE*, vol. 42, no. 14, pp. 5089-5103, Jul. 2022.
[27] L. Liu, Y. Wang, Y. Liu *et al*., "Analysis of sub-synchronous interaction mechanism between D-PMSG based wind farm and LCC-HVDC," in *Proceedings of 2021 IEEE Sustainable Power and Energy Conference*, Nanjing, China, Dec. 2021, pp. 203-210.
[28] B. Gao, P. Deng, Y. Wang *et al*., "Evaluation of damping of subsynchronous interaction between direct-drive wind farm and LCC-HVDC based on the damping path analysis," *International Journal of Electrical Power &Energy Systems*, vol. 144, pp. 108532-108542, Jan. 2023.
[29] B. Gao, Y. Liu, R. Song *et al*., "Study on subsynchronous oscillation characteristics of DFIG-based wind farm integrated with LCC-HVDC system," *Proceedings of the CSEE*, vol. 40, no. 11, pp. 3477-3489, Jun. 2020.
[30] B. Gao, Y. Liu, B. Shao *et al*., "A path analysis method to study the subsynchronous oscillation mechanism in direct-drive wind farm with VSC-HVDC system," *International Journal of Electrical Power & Energy Systems*, vol. 142, pp. 108328-108341, May 2022.
[31] H. Weng, Y. Xu, and Z. Wang, "The impact of steam-turbine governor system on the low frequency oscillation of power grids," *Southern Power System Technology*, vol. 8, no. 3, pp. 83-86, Jun. 2014.
[32] Y. Xu, M. Zhang, L. Fan *et al*., "Small-signal stability analysis of type-4 wind in series-compensated networks," *IEEE Transactions on Energy Conversation*, vol. 35, no. 1, pp. 529-538, Mar. 2018.
[33] S. Zhao, N. Wang, R. Li *et al*., "Sub-synchronous control interaction between direct-drive PMSG-based wind farms and compensated grids," *International Journal of Electrical Power & Energy Systems*, vol. 109, pp. 609-617, Jul. 2019.

Shiying Ma received the B. S. degree from Xi'an Jiaotong University, Xi'an, China, in 1990, and the M.S. and Ph.D. degrees in electrical engineering from China Electric Power Research Institute, Beijing, China, in 1996 and 2013, respectively. He is currently the Deputy Director of Power System Department. His research interests include power system dynamics, stability, and control.

Liwen Zheng received the B.S. degree from Yanshan University, Yanshan, China, in 2018, and the M.S. degree in electrical engineering from North China Electric Power University, Baoding, China, in 2021. She is currently pursuing the Ph.D. degree in the Power System Department, China Electric Power Research Institute, Beijing, China. Her research interests include power system stability and control.